

<https://doi.org/10.1038/s41612-024-00720-3>

Contribution of anthropogenic influence to the 2022-like Yangtze River valley compound heatwave and drought event

Check for updates

Dong Chen¹, Shaobo Qiao^{1,2} , Jie Yang^{1,3}, Shankai Tang^{1,4} , Dongdong Zuo⁵ & Guolin Feng^{1,6}

In August 2022, an unprecedented compound heatwave and drought event (CHDE) lasting 24 days occurred in the Yangtze River valley (YRV), leading to a severe reduction of the crop, fresh water, and power supply. We constructed a joint cumulative probability distribution of heatwave and drought intensity, and found that the lowest probability-based index (PI) of 0.06 in 2022 was estimated as a 1-in-662-year event over the 1961–2022 climate. We then detected the fingerprint of greenhouse gas forcing to the observed PI in a generalized extreme value framework, but not the aerosol forcing, suggesting the leading contribution of greenhouse gas forcing on such extreme CHDE. Furthermore, anthropogenic influence had increased the probability of such CHDE by more than 10 times compared to the counterfactual climate. Also, the PI decreased from about 0.30 at the present climate to about 0.14 at the 3 °C global warming level, indicating that CHDE will become more extreme over YRV.

Extreme climate and weather events can destroy the ecosystems and economies, which are the major concern for human society¹. When extreme events occur simultaneously or consecutively, they have greater damage to the society and environment than individual extreme events, which is called compound extreme event². As the most common type of compound extreme events, the occurrence of compound heatwave and drought event (CHDE) is closely associated with the thermodynamic negative relationship between temperature and rainfall². Usually, the persistent heatwave events always cause moisture deficiency and low rainfall, and result in severe drought³. On the other hand, the drought increases (decreases) the releases of atmospheric sensible (latent) heat, further promoting the intensity of heatwave events^{4–6}. Under the global warming background, the CHDE frequency represents a significant increase tendency over the most global land area from the past period (1983–1999) to the relatively warmer recent period (2000–2016)⁷, accompanied by an increased occurrence probability of such events in future climate projections^{8–10}, which has proved to be the most harmful compound extreme events that produce threat on agriculture, water availability, energy production, and human health^{11–15}. For example, in the summer of 2010, CHDE in Russia caused an estimated 55,000 deaths, a drop of 25% in annual crop production, and more than one million hectares burned areas^{16,17}.

Considering the possible increase of CHDE in response to human-induced global warming, there is an urgent need to reveal the contribution of anthropogenic influence to the CHDE. How is the CHDE detected and attributed? First, it is important to define CHDE using an appropriate method. Numerous studies have defined the CHDE according to different combinations, such as the composite index of rainfall and surface air temperature (SAT)¹⁸, the composite anomalies of meteorological drought and SAT¹⁹, and the combined deficit of potential evapotranspiration and rainfall²⁰. After these CHDE indices were constructed via the bivariate copula method^{21,22} or time of emergence method²³, we then could estimate the intensity or frequency of CHDE in both observations and climate model simulations under different forcings and conduct the detection and attribution analysis. For example, Pan et al.²⁴ used the bivariate copula method to define CHDE and demonstrated that anthropogenic climate change had significantly increased the likelihood of summer CHDE in six continents of the world. Zhang et al.²⁵ also evidenced that anthropogenic forcing had contributed to the increased CHDE over the global land areas, with the increasing trend exceeding 0.17/decade from 1951 to 2010, while the trend of CHDE was merely –0.008/decade under natural forcing. However, when the attribution analysis was conducted for the heatwave and drought events separately, the occurrence probability of heatwave events was always higher than those of drought events under anthropogenic forcing than natural

¹School of Atmospheric Sciences Sun Yat-Sen University, and Southern Marine Science and Engineering Guangdong Laboratory (Zhuhai), Zhuhai, China. ²Key Laboratory of Meteorological Disaster (KLME), Ministry of Education & Collaborative Innovation Center on Forecast and Evaluation of Meteorological Disasters (CIC-FEMD), Nanjing University of Information Science & Technology, Nanjing, China. ³Meteorological Administration Key Open Laboratory of Transforming Climate Resources to Economy, Chongqing, China. ⁴College of Atmospheric Sciences, Lanzhou University, Lanzhou, China. ⁵School of Environmental Science and Engineering, Yancheng Institute of Technology, Yancheng, China. ⁶School of Physical Science and Technology, Yangzhou University, Yangzhou, China.

e-mail: qiaoshb3@mail.sysu.edu.cn

forcing, and thus the occurrence probability of CHDE tended to be lower (higher) than heatwave (drought) event²². As such, it is important to select an appropriate method to define the CHDE for the regions that we are concerned with, which is an essential precondition for robust detection and attribution results.

In the summer of 2022, several regions over the Northern Hemisphere suffered from record-breaking heatwave and drought events, including the Yangtze River valley (YRV) in China²⁶, western Europe²⁷, western America²⁸, and the Horn of Africa²⁹. Specifically, the YRV experienced an unprecedented CHDE during the summer of 2022 that lasted from early August until the end of August (Fig. 1a, c), with the duration of the heatwave event and drought event at more than 530 and 180 stations over the YRV setting the longest records since 1961, respectively (Supplementary Fig. 1). Such a CHDE led to hydrological droughts and electricity shortages, which affected more than 4.08 million hectares of crops, 4.3 million people and 350,000 livestock³⁰. As suggested by recent studies, the individual heatwave event was rarer than the drought event over the YRV in 2022 summer according to the historical observations¹⁸, which corresponded to a more significant response of the heatwave event to the anthropogenic influence than the drought event, with an increasing occurrence probability of such a heatwave event under anthropogenic forcing than natural forcing by about 11 times³¹. Despite we have a general understanding of a much larger increase in the occurrence probability of heatwave events than drought events in response to the ongoing global warming, comparing the response of August 2022-like CHDE in the YRV that contains the heatwave and drought events at the same time to different external forcings remains a

puzzle. Thus, in this study, we focus on the following questions: Whether anthropogenic forcing as a whole and individual forcing (e.g., anthropogenic aerosols and greenhouse gases) have imposed a detectable influence on the August 2022-like CHDE over the YRV? How will the likelihood of such events change in the future?

In this study, we found that anthropogenic forcing had increased the probability of CHDE as severe as the 2022 case over the YRV by more than 10 times over the present climate, which will become more frequent and severe under medium emissions in the future. Our results will provide a reference for understanding and preparing for compound extreme events in East Asia.

Methods

Observational and model-simulated data

We obtained the daily surface maximum temperature (T_{max}) and rainfall datasets from the National Meteorological Information Center of China, which covered 751 meteorological stations over the YRV from 1961 to 2022^{32,33}. The simulations of the two variables from 9 climate models were acquired from phase 6 of the Coupled Model Intercomparison Project (CMIP6)³⁴. Each model included simulations based on all external (ALL) forcing, greenhouse gas (GHG) forcing, anthropogenic aerosol (AER) forcing, and natural (NAT) forcing, as well as at least three ensemble members for each simulation (Table 1). The selection of all 9 models was due to that a much larger model spread can cover the observed PI as much as possible, with the multi-model ensemble close to the observations. The ALL forcing simulations that ended in 2014 were extended to 2022 using shared

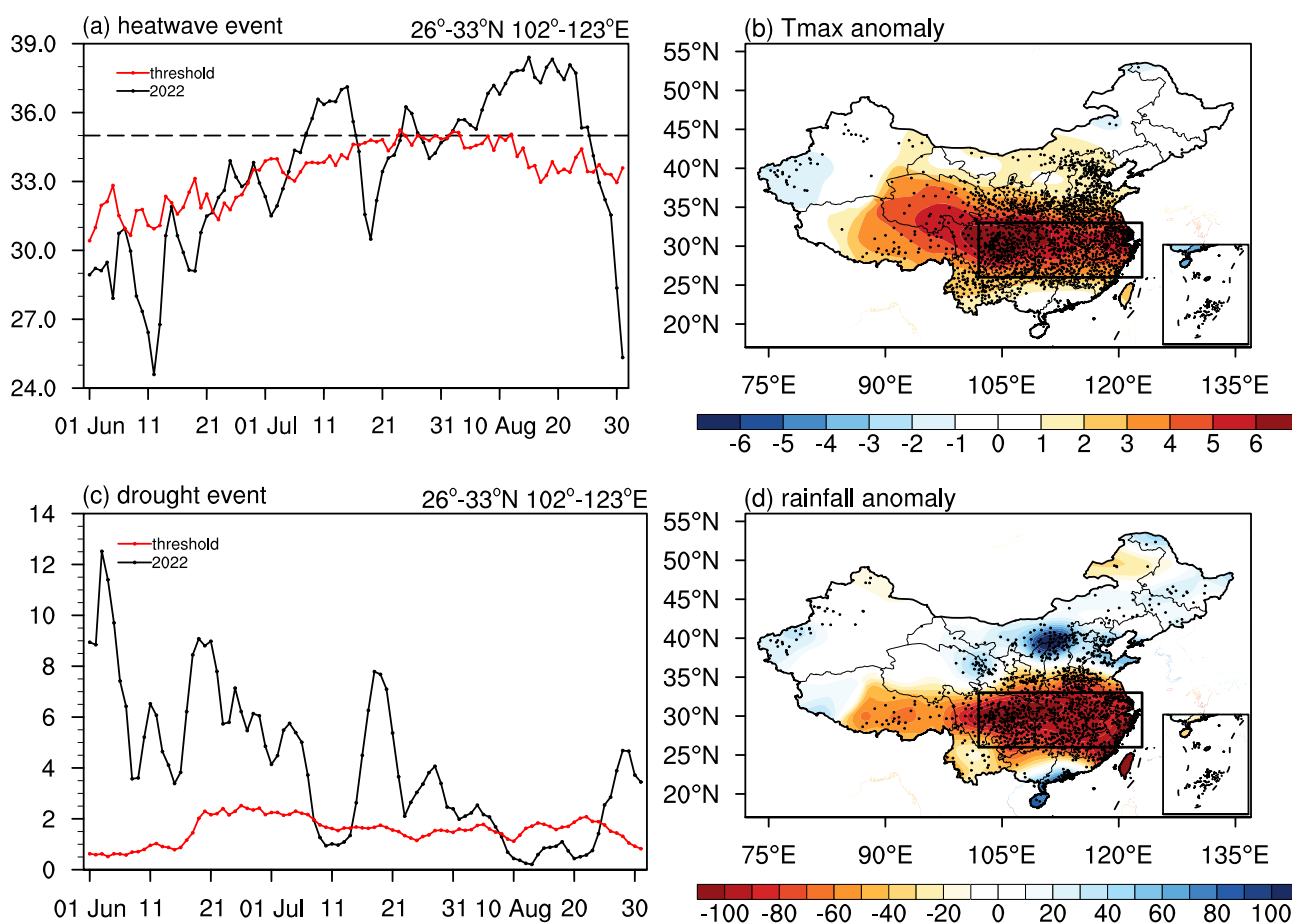


Fig. 1 | The 2022 summer (June–July–August) T_{max} and rainfall anomalies relative to the 1981–2010 climatology. Evolution of (a) the T_{max} and c the 5-day running-mean rainfall averaged over the YRV (26°–33° N, 102°–123° E) during the 2022 summer (black line). **b** The observed T_{max} anomalies (unit, °C) and

d accumulated rainfall anomalies (unit, mm) averaged between August 2 and August 25. The red line indicated the threshold of the T_{max} and rainfall in (a, c), and the dashed line represented 35 °C in (a). Stippling indicates exceeding one standard deviation.

Table 1 | List of CMIP6 models and simulations used in this article, together with their horizontal resolutions

Model name	Merged historical and SSP2–4.5 simulations	Historical NAT simulations	Historical aerosol simulations	Historical GHG simulations	Horizontal resolution
ACCESS-CM2	3	3	3	3	1.25 × 1.88
ACCESS-ESM1-5	5	3	3	3	1.25 × 1.88
CanESM5	25	10	10	10	2.81 × 2.81
FGOALS-g3	3	3	3	3	2.25 × 2.00
HadGEM3-GC31-LL	4	4	4	4	1.25 × 1.88
IPSL-CM6A-LR	4	6	6	6	1.26 × 2.50
MIROC6	24	3	10	25	1.41 × 1.41
MRI-ESM2-0	5	5	5	5	1.12 × 1.12
NorESM2-LM	3	3	3	3	1.88 × 2.50

Also shown is the ensemble size of simulations in historical, SSP2–4.5, aerosol, GHG, and NAT.

socioeconomic pathway2–4.5 (SSP2–4.5) simulations³⁵, and the other forcing simulations that ended in 2020 were extended to 2022 by repeating data from 2019 to 2020^{36,37}. The CMIP6 simulations were interpolated to the same spatial resolution of 2° × 2° through area-weighted averaging prior to analysis.

Definition of CHDE

The heatwave and drought events were respectively identified when the daily T_{max} exceeded the 90th percentile and daily rainfall below the 10th percentile for at least five consecutive days during the summer (June–July–August)^{8,25,38,39}. Note that a 5-day running mean had been conducted to the daily rainfall before analysis due to its unevenness. Then we used the bivariate copula method to construct the joint cumulative probability distribution of heatwave and drought to define CHDE^{21,22,40–42}. Based on this method, heatwave and drought could be considered simultaneously, which helps to identify the severity of CHDE and has been used to conduct the detection, attribution, and projection^{21,42}. The copula model (C) of heatwave (X) and drought (Y) can be defined as⁴³:

$$F(x, y) = C[F(X), G(Y)] \tag{1}$$

where $F(X) = P(X \leq x)$ and $G(Y) = P(Y \leq y)$ were marginal cumulative probability distributions of heatwave and drought events, respectively. Here, the x and y represented the threshold of heatwave events and drought events, respectively. The $F(X)$ can be regarded as the probability of neither a heatwave event nor a drought event. Then, the complementary part of their cumulative probability can be defined as:

$$PI = P(X \geq x, Y \geq y) = 1 + C[F(X), G(Y)] - F(X) - G(Y) \tag{2}$$

where the PI can denote the severity of CHDE, which ranges from 0 to 1, with a higher (lower) PI representing a weaker (stronger) CHDE¹. Based on previous studies^{44–46}, the exponential and gamma distributions were chosen to calculate the marginal cumulative probability distributions of the heatwave and drought event, respectively. Besides, the three Archimedean copulas applied in this study are as follows⁴⁷:

(1) Clayton copula

$$C_{\theta}(u, v) = (u^{-\theta} + v^{-\theta} - 1)^{-1/\theta}, \theta \in [0, +\infty) \tag{3}$$

(2) Frank copula

$$C_{\theta}(u, v) = -\frac{1}{\theta} \ln \left(1 + \frac{(e^{-\theta u} - 1)(e^{-\theta v} - 1)}{e^{-\theta} - 1} \right), \theta \neq 0 \tag{4}$$

(3) Gumbel copula

$$C_{\theta}(u, v) = e^{\left\{ -[(-\ln u)^{\theta} + (-\ln v)^{\theta}]^{1/\theta} \right\}}, \theta \in [1, +\infty) \tag{5}$$

Further, we used the root mean square error (RMSE), the Akaike information criterion (AIC), and the Kolmogorov–Smirnov statistic D_n to choose the optimal copula method. The RMSE, AIC, and D_n are expressed as:

$$RMSE = \sqrt{\frac{1}{n} \sum_{i=1}^n (C_p(i) - C_e(i))^2} \tag{6}$$

$$AIC = n \ln MSE + 2m \tag{7}$$

$$D_n = \sup |C_p(i) - C_e(i)| \tag{8}$$

where n is the sample size; C_p denotes the computed values of the parametric copula; C_e denotes the observed values of the probability obtained from the empirical copula; $\ln MSE$ denotes the mean square error; m is the number of independently adjusted parameters; and \sup denotes the upper bound. The model is more efficient when RMSE, AIC, and D_n are smaller. As shown in Supplementary Table 1, the RMSE, AIC, and D_n for the considered copulas were compared. Based on the comparison it was determined that the Gumbel copula had minimum RMSE, AIC, and D_n among all of the considered copulas. Therefore, the Gumbel copula was selected to construct the joint cumulative probability distribution of heatwave and drought.

Optimal fingerprinting method

Based on the generalized extreme value (GEV) distribution, the optimal fingerprinting method was used to assess whether anthropogenic forcing was detectable in the 1961–2022 CHDE observations^{48,49}. The cumulative distribution function for a GEV distributed $G(z)$ is given by Coles⁵⁰:

$$G(z) = \exp \left[- \left(1 + \xi \frac{z - \mu}{\sigma} \right)^{-1/\xi} \right], 1 + \xi \frac{z - \mu}{\sigma} > 0 \tag{9}$$

where $\mu, \sigma > 0$, and ζ are the location, scale, and shape parameters, respectively. The probability-weighted moments are adopted to estimate these parameters, which is more robust than maximum likelihood estimation for relatively short samples⁵¹. Then, the optimal fingerprinting method of the climate model simulated response X of the extreme event to the external forcing is expressed as:

$$y_{s,t} = c_s + X_{s,t} \beta \tag{10}$$

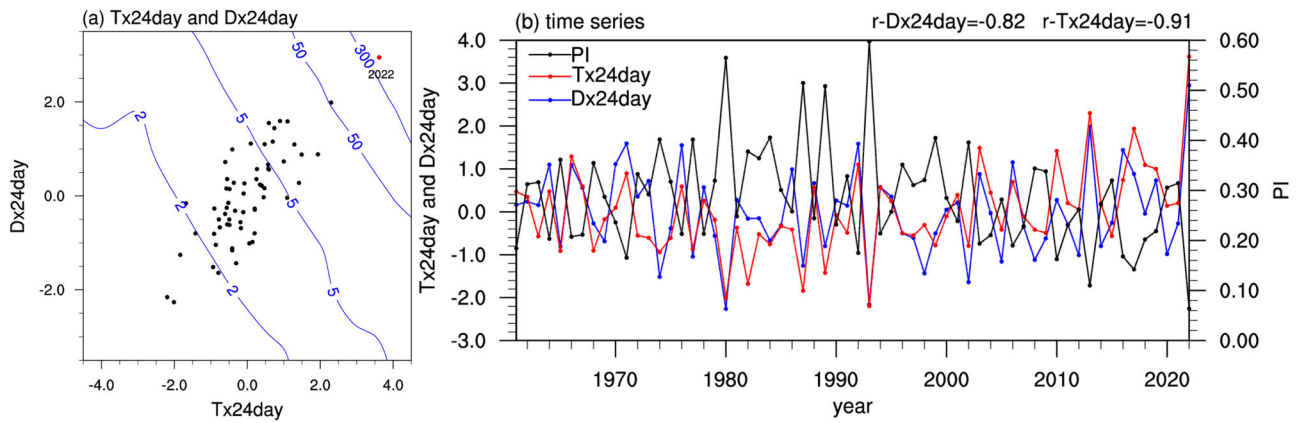


Fig. 2 | The extremity of CHDE over the YRV (26°–33° N, 102°–123° E) during the 2022 summer. **a** Scatterplot of the Tx24day and Dx24day averaged over the YRV for the period of 1961–2022 summers in observations. **b** Evolution of the normalized Tx24day (red line), Dx24day (blue line), and the associated PI (black line) during the 1961–2022 summers. The red dot indicates the year of 2022, and the isolines are for the return period in **(a)**. The correlations between the PI and the Tx24day (Dx24day) are indicated at the top right in **(b)**. Note that the climatology is based on the period 1981–2010.

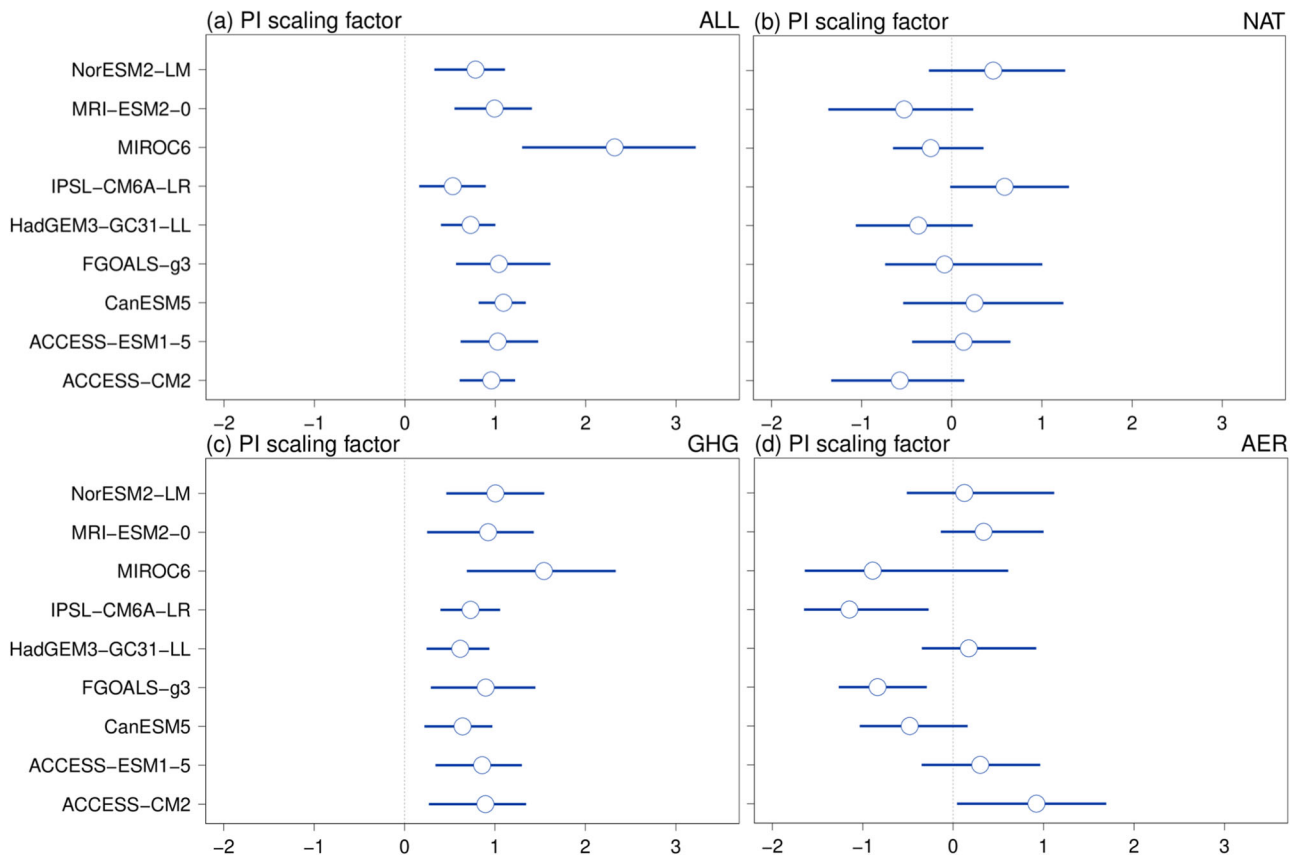


Fig. 3 | The scaling factors of PI under different external forcings. Best estimation and 5–95% CI of the scaling factors from fingerprinting analyses of PI over the YRV during 1961–2022 summers under **a** ALL, **b** NAT, **c** GHG, and **d** AER forcings. The dots and error bars indicate the best estimation and the 5–95% CI.

where y represented the observed extreme event, c denoted the internally generated residual variability, and β was the scaling factor that was estimated by a total square method. Subscripts s and t denoted the region and time, respectively. By assuming that the spatiotemporal patterns of model responses were identical to the observations, we can obtain the β which was suitable for the whole region. Furthermore, a two-stage spatiotemporal block bootstrap procedure was used to estimate the uncertainty of the β due to the internal variability in models and observations⁴⁸. Because the automated identification approaches were subject to uncertainty from

sampling variability, and the statistical procedures for the detection of spatial inhomogeneity may not be much efficient³², the model simulations were interpolated to the same spatial resolution of $5^\circ \times 5^\circ$ to conduct the optimal fingerprinting method.

Estimation of the risk of CHDE

The occurrence frequency p of an event with intensity x can be estimated by the probability of exceeding x in the fitted GEV distribution, and the return period T can be expressed as $T = 1/p$. Also, the probability ratio (PR) was

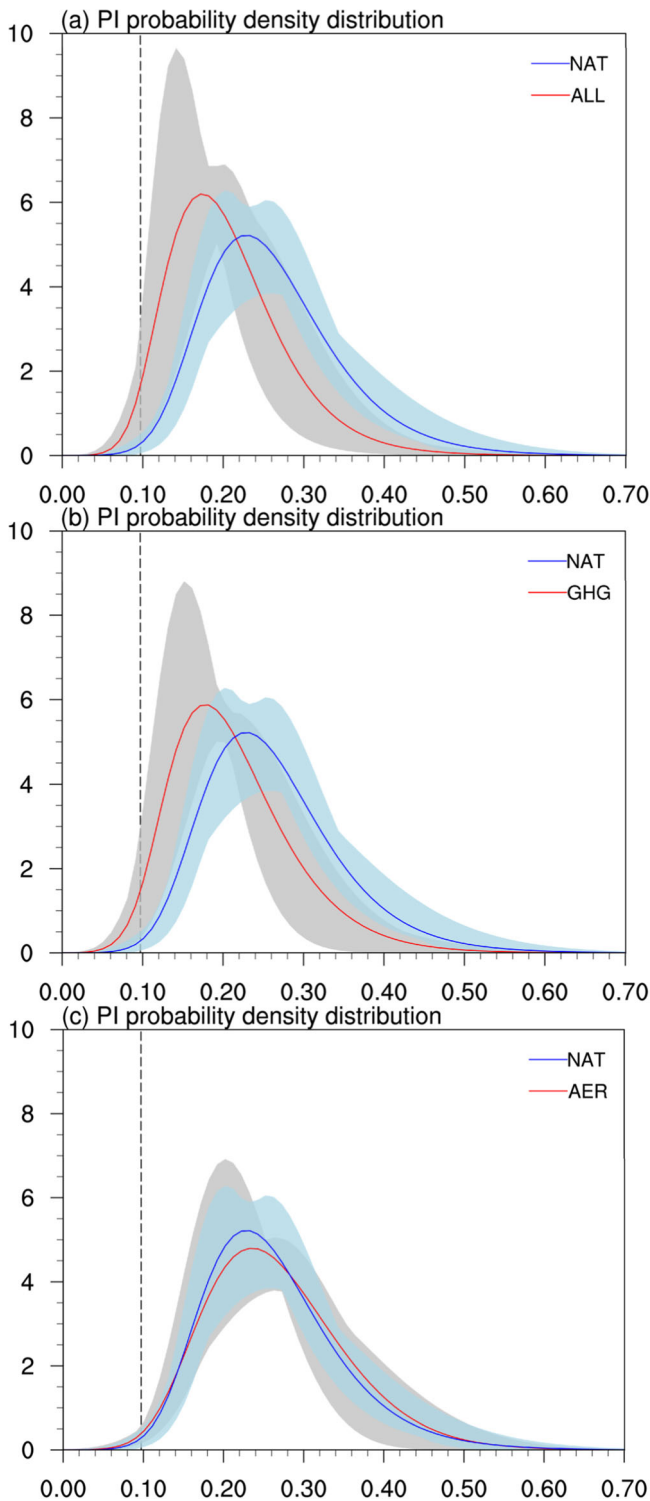


Fig. 4 | The PDF of PI under different external forcings. PDF of PI over the YRV during 2000–2022 summers under NAT, **a** ALL, **b** GHG, and **c** AER forcings. Note that shading denotes the range of ensemble models under NAT forcings (blue) and other forcings (gray), and the dashed line denotes the threshold of observed PI.

used to quantify the extent of anthropogenic influence on the likelihood of extreme events as the one observed over the YRV during 2022⁵³. The PR was expressed as: $PR = p_1/p_0$, where p_1 and p_0 were the probabilities of extreme events as severe as the observed one under external forcing and NAT force, respectively.

Results

Identification and evolution of the CHDE in 2022

Figure 1a shows the evolution of observed T_{max} averaged over the YRV (26°–33° N, 102°–123° E) during the 2022 summer. It was found that a long-lasting heatwave event occurred over the YRV in August, which started on August 2 and ended on August 25 with a duration of 24 days (Fig. 1a). Simultaneously, the persistent heatwave induced a severe drought event over the YRV, with the regional-mean rainfall below the 10th percentile persisting 17 days from August 8 to August 24 (Fig. 1c). This was a typical high-intensity and long-lasting CHDE, accompanied by the T_{max} anomalies and accumulated rainfall deficit anomalies during 2–25 August 2022 averaged over the YRV exceeding 6.0 °C (Fig. 1b) and 100 mm (Fig. 1d), respectively. Accordingly, we used the normalized values of maximum T_{max} (Tx24day) and rainfall deficit anomalies (Dx24day) for 24 consecutive days in summer to represent the severity of such a CHDE as the 2022 one^{54,55}. To facilitate the analysis of the concurrent events, the Dx24day was defined as the 24-day rainfall anomalies accumulation multiplied by (−1) to ensure the in-phase linkage with the Tx24day. In the following, we will elaborate on how the likelihood of such CHDE over the YRV has changed in response to the anthropogenic forcing as a whole and to individual forcings such as anthropogenic aerosols and greenhouse gases.

To represent the extremity of the CHDE in the 2022 summer across the historical period, Fig. 2a showed the scatterplot of the normalized Tx24day and Dx24day averaged over the YRV during the 1961–2022 summers. We can see that the Tx24day and Dx24day were between −2 and 2 in majority years, and both indices in 2022 set the highest historical record since 1961 (Fig. 2a). Correspondingly, the probability-based index (PI) had a lowest value of 0.06, with a return period of about 662 years (106 to >10,000 years for 5–95% confidence interval (CI); Supplementary Fig. 2) during the historical period, more than 10 times larger than the return period (~50 years) of PI (0.10) in 2013 summer, which ranked the second strongest CHDE since 1961 (Fig. 2). On the other hand, the PI presented a stronger correlation with the Tx24day than Dx24day, where the correlation coefficients between the PI and the two indices were −0.91 and −0.82, respectively (all exceed the 99.9% CI; Fig. 2b). Also, the decreasing trend of the PI (−0.013/decade) since 1961 indicated that the CHDE over the YRV have become more extreme against the background of the ongoing global warming, which was consistent with the increasing trend of the Tx24day (0.2/decade) and different from the observed Dx24day trend of near 0 during the same period. Note that the results were almost unchanged if we used the Tx17day and Dx17day in each summer to construct the PI (Supplementary Fig. 3). These results suggested a stronger contribution to the CHDE by the heatwave event than drought event over the YRV.

Detection and attribution of the CHDE in 2022

Based on the fingerprinting method designed particularly for climate extremes, we compared the observed and climate models simulated time series of PI during 1961–2022 summers to detect the possible anthropogenic influence on the CHDE over the YRV under different external forcings, as shown in Fig. 3. The 5–95% CIs of the scaling factors exceeded 0 for all nine models under ALL forcings (Fig. 3a), indicating that the anthropogenic forcing signals were well detected. The estimated scaling factors under GHG forcings were almost the same as under ALL forcings (Fig. 3a vs c), which can well detect the role of GHG forcings in the observed change of CHDE over the YRV during the historical period. In contrast, the 5–95% CIs of the scaling factors of the PI were not significantly different from 0 for eight models under NAT forcings and AER forcings, suggesting a much weaker role of the nature variability and aerosol forcings to CHDE (Fig. 3b, d). Again, the detection results of PI were quite similar to those of Tx24day anomalies rather than Dx24day anomalies (Fig. 3 vs Supplementary Fig. 4 and Fig. 3 vs Supplementary Fig. 5), so the human-induced increase of heatwave event accounted for the leading contributions to the more extreme CHDE in response to the ongoing global warming. Overall, the fingerprinting analyses detected the significant impact of anthropogenic global

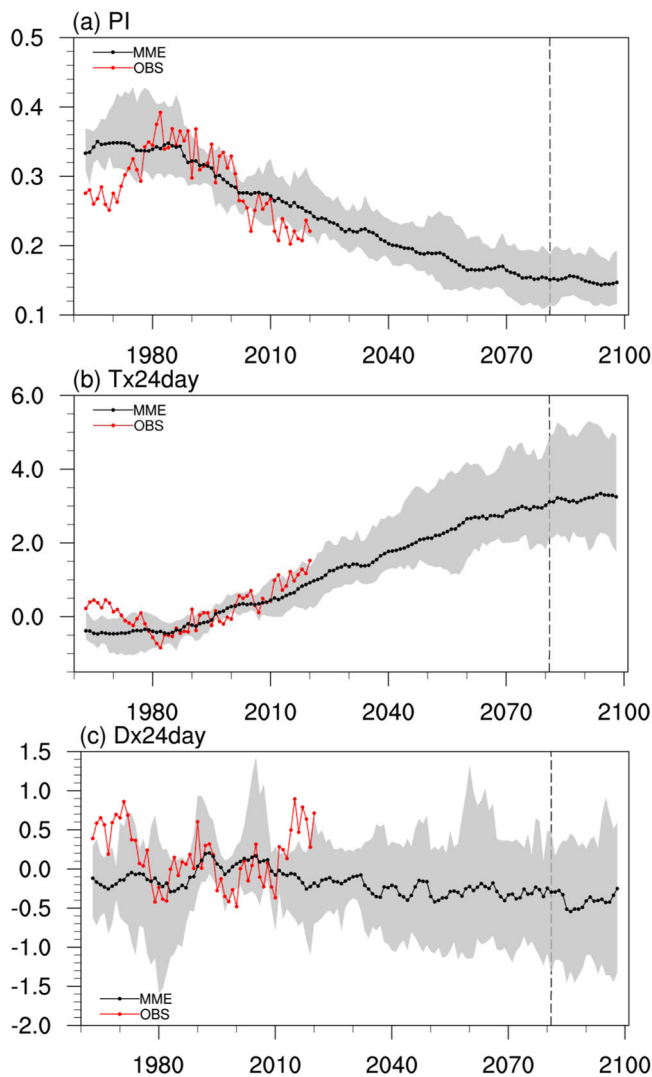


Fig. 5 | The future projection of PI, Tx24day anomalies, and Dx24day anomalies. The 5-year running-mean of the summertime (a) PI, b Tx24day anomalies, and c Dx24day anomalies averaged over the YRV from 1961 to 2100 in observations (red line) and CMIP6 multi-model ensemble mean (black line). The historical period (1961–2014) and the future period (2015–2100) are based on historical ALL forcings and SSP2–4.5 simulations, respectively. Note that shading denotes the range of ensemble models, and the climatology is based on the period 1981–2010.

warming on the CHDE like the 2022 case over the YRV, which was largely contributed by the GHG forcings.

Furthermore, we quantified the probability of extreme CHDE as severe as the 2022 case over the YRV in different external forcings under the present climate of 2000–2022 summers. The probability density function (PDF) of PI under ALL forcings was more skewed to the left than under NAT forcings, representing a higher probability of the occurrence of extreme CHDE in response to the ongoing global warming (Fig. 4a). Because the considered 9 climate models were unable to simulate the observed PI of 0.06 in 2022 under NAT forcings, we fitted the GEV distribution using the observed PI during 1961–2022 summers and chose the 1st percentile of 0.10 as the threshold to compare the occurrence probability of extreme CHDE under different forcings. The likelihood of PI lower than the threshold was 2.74% (5–95% CI: 1.91–3.80%) under ALL forcings and 0.47% (5–95% CI: 0.24–0.58%) under NAT forcings, corresponding to an estimated probability ratio (PR_{ALL}) of 9.92 (5–95% CI: 6.59–17.00) between ALL forcings and NAT forcings (Fig. 4a). The PDF of the PI under the GHG

forcings was similar with that under ALL forcings, which showed a pronounced leftward shift compared to that under NAT forcings with an estimated PR_{GHG} of 11.66 (5–95% CI: 7.50–21.67) (Fig. 4b). Although the PDF of the PI under the AER forcings represented a similar structure with the NAT forcings, the probability of PI lower than the threshold (0.73% (5–95% CI: 0.56–0.85%)) under the AER forcings was slightly larger than NAT forcings (0.47% (5–95% CI: 0.24–0.58%)) (Fig. 4c). Note that both PR_{ALL} and PR_{GHG} obviously increased when we improved the extremity of the observed threshold from 5th to 1st percentile (Supplementary Table 2). It suggested that the anthropogenic forcings had increased the probability of the CHDE over the YRV as severe as the 2022 one (<0.2 percentile) by more than 10 times compared to NAT forcings under the present climate, and GHG forcing played a dominant role. Also, if we repeated the results under the climate of 1961–2022 summers, the probability of such an event under ALL forcings and GHG forcings was considerably larger than NAT forcings (Supplementary Fig. 6), despite a lower PR_{ALL} and PR_{GHG} than those under the climate of 2000–2022 summers (Fig. 4 vs Supplementary Fig. 6). In summary, the August 2022-like CHDE was impossible in the pre-industrial climate and exceptionally rare even now, but the likelihood of such CHDE had already increased due to anthropogenic climate change.

Projection of the CHDE in the future

On the basis of understanding the crucial role of anthropogenic influence to the extreme CHDE like the 2022 case, we further investigated the changes in the severity of CHDE over the YRV in the future. Accordingly, Fig. 5 shows the 5-year running-mean time series of observed PI, Tx24day anomaly, and Dx24day anomaly during the 1961–2022 summers, as well as the three variables simulated by the climate models from 1961 to 2100. These simulations for the periods of 1961–2014 and 2015–2100 were derived from historical ALL forcings and SSP2–4.5 simulations, respectively. It was found that the PI increased from the 1960s to early 1980s and decreased afterward in observations (Fig. 5a), which primarily resulted from the decreasing (increasing) tendency of the persistent heatwave intensity before (after) the early 1980s (Fig. 5b). The considered climate models had large biases in simulating the evolution of PI and Tx24day anomaly during the 1960s and 1970s, and well simulated the downward (upward) trend of the PI (Tx24day anomaly) since the 1980s (Fig. 5a, b). Furthermore, we projected the future change of PI and Tx24day anomaly averaged over the YRV under SSP2–4.5 simulations, and found that the considered climate models represented a consistently decreasing PI from about 0.30 at present climate to about 0.14 at a global warming level of 3 °C (relative to climatology in CMIP6 models) (Fig. 5a, b and Supplementary Fig. 7), accompanied by a more and more leftward (rightward) shift of the PI (Tx24day anomaly) in the subsequent 20-year moving windows during 2021–2100 (Supplementary Fig. 8a, b). The estimated PR_{SSP} was about 38.60 (5–95% CI: 24.14–68.28) at the 3 °C global warming level relative to NAT forcings (Supplementary Fig. 8a). On the other hand, the considered climate models did not reproduce the evolution of observed Dx24day anomalies during the historical period, particularly for the periods before the 1980s and since 2010s (Fig. 5c). The projected Dx24day anomaly showed a slight decrease with large uncertainty in the future (Fig. 5c), with the PDFs appearing little difference between the SSP2–4.5 simulations during 2021–2100 and NAT forcings during the present climate (Supplementary Fig. 8c). Therefore, the heatwave events provided a dominant contribution to the CHDE over the YRV in the future, and the persistently decreasing of PI caused the CHDE more and more extreme.

Discussion

The YRV experienced a long-lasting CHDE from 2 to 25 August 2022 with a duration of 24 days. Both maximum temperature anomalies over 24 days (Tx24day) and rainfall deficit anomalies over 24 days (Dx24day) in the 2022 summer set the highest historical record in the past 60 years. Accordingly, we constructed a PI using the joint cumulative probability

distribution of Tx24day and Dx24day in summer to measure the intensity of CHDE, and found that the 2022 CHDE was regarded as the strongest CHDE with the lowest PI (0.06) since 1961 and the longest return period of about 662 years (106 to >10,000 years for 5–95% CI) over 1961–2022 climate. Based on the fingerprinting method designed particularly for climate extremes, we detected the signals of the anthropogenic forcings on the observed PI time series during 1961–2022, but not the NAT forcing and AER forcing, suggesting the leading contribution of GHG forcing on such extreme CHDE.

Subsequently, we quantified the anthropogenic influence to the likelihood of the extreme CHDEs as severe as the 2022 case over the current 2000–2022 climate, and found a pronounced leftward shift of the PI's PDF under the ALL (GHG) forcings relative to NAT forcings, while the probability of PI lower than the threshold was almost the same under AER forcings and NAT forcings. In other words, the anthropogenic forcings had significantly increased the probability of the CHDE over the YRV as severe as 2022 by more than 10 times compared to NAT forcings under the present climate, with GHG forcing providing a dominant contribution. Also, we projected the changes in the severity of CHDE over the YRV under SSP2–4.5 simulations in the future, and found the PI represented a persistently decreasing trend from about 0.30 at the present climate to about 0.14 at a global warming level of 3 °C (relative to climatology in CMIP6 models), which primarily resulted from the increasing tendency of the persistent heatwave intensity and indicated that CHDE will become more extreme in the future.

To highlight the importance of the heatwave event to the CHDE, the Dx24day in each summer was calculated based on the same period of Tx24day in the present study. This is because the drought event was induced by the persistent heatwave event over the YRV in August 2022, due to the fact that the heatwave event had a longer duration and started (ended) earlier (later) than the drought event (Fig. 1). As a result, the drought event may not be the strongest one during some summers, leading to an underestimation of the CHDE intensity. When using the strongest Tx24day and the strongest Dx24day in each summer to construct the PI, we found the results were almost unchanged, as evidenced by the correlation coefficient between the two-time series of PI during the 1961–2022 summer to be 0.96 (Supplementary Fig. 9).

Previous studies have suggested that the internal variability was the main factor leading to the CHDE over YRV in 2022 summer^{26,56–58}, and we further verified that such an event will become more common under the background of GHG forcing despite large uncertainties still remaining in this study. On one hand, the considered 9 climate models were unable to simulate the observed PI of 0.06 in 2022 under NAT forcings, and we chose the 1st percentile of the observed PI of 0.10 during the 1961–2022 summers as the threshold instead. On the other hand, much larger biases originated from the simulated variability of drought than heatwave in these climate models (Fig. 5b vs c). Thus, we would like to analyze more large ensemble simulations that covered the observed threshold to reduce the uncertainties of the current results, and use the observed heatwave–drought relationship to constrain the future change of the drought and CHDE intensity over the YRV in the future study.

Data availability

The CMIP6 model data were downloaded from <https://esgf-node.llnl.gov/projects/cmip6/>. The observational data were available from <http://data.cma.cn/en>.

Code availability

All Figures in this article are produced by the NCAR Command Language (NCL) version 6.4.0, and the source codes can be obtained upon request to the corresponding authors.

Received: 2 February 2024; Accepted: 15 July 2024;

Published online: 23 July 2024

References

- Li, H. X., Chen, H. P., Sun, B., Wang, H. J. & Sun, J. Q. A detectable anthropogenic shift toward intensified summer hot drought events over northeastern China. *Earth Space Sci.* **7**, e2019EA000836 (2020).
- Zscheischler, J. et al. Future climate risk from compound events. *Nat. Clim. Change* **8**, 469–477 (2018).
- Dai, A., Trenberth, K. E. & Qian, T. T. A global dataset of Palmer drought severity index for 1870–2002: relationship with soil moisture and effects of surface warming. *J. Hydrometeorol.* **5**, 1117–1130 (2004).
- Seneviratne, S. I., Lüthi, D., Litschi, M. & Schär, C. Land-atmosphere coupling and climate change in Europe. *Nature* **443**, 205–209 (2006).
- Mueller, B. & Seneviratne, S. I. Hot days induced by precipitation deficits at the global scale. *Proc. Natl. Acad. Sci. USA* **109**, 12398–12403 (2012).
- Greve, P. et al. Global assessment of trends in wetting and drying over land. *Nat. Geosci.* **7**, 716–721 (2014).
- Mukherjee, S. & Mishra, A. K. Increase in compound drought and heatwaves in a warming world. *Geophys. Res. Lett.* **48**, e2020GL090617 (2021).
- Hao, Z. C., AghaKouchak, A. & Phillips, T. J. Changes in concurrent monthly precipitation and temperature extremes. *Environ. Res. Lett.* **8**, 034014 (2013).
- Mazdiyasn, O. & AghaKouchak, A. Substantial increase in concurrent droughts and heatwaves in the United States. *Proc. Natl. Acad. Sci. USA* **112**, 11484–11489 (2015).
- Sharma, S. & Mujumdar, P. Increasing frequency and spatial extent of concurrent meteorological droughts and heatwaves in India. *Sci. Rep.* **7**, 15582 (2017).
- Mishra, A. K. & Singh, V. P. A review of drought concepts. *J. Hydrol.* **391**, 204–216 (2010).
- Deryng, D., Conway, D., Ramankutty, N., Price, J. & Warren, R. Global crop yield response to extreme heat stress under multiple climate change futures. *Environ. Res. Lett.* **9**, 034011 (2014).
- Zipper, S. C., Qiu, J. X. & Kucharik, C. J. Drought effects on US maize and soybean production: spatiotemporal patterns and historical changes. *Environ. Res. Lett.* **11**, 094021 (2016).
- Añel, J. A., Fernández-González, M., Labandeira, X., López-Otero, X. & de la Torre, L. Impact of cold waves and heat waves on the energy production sector. *Atmosphere* **8**, 209 (2017).
- Dosio, A., Mentaschi, L., Fischer, E. M. & Wyser, K. Extreme heat waves under 1.5 °C and 2 °C global warming. *Environ. Res. Lett.* **13**, 054006 (2018).
- Barriopedro, D., Fischer, E. M., Luterbacher, J., Trigo, R. & Garcia-Herrera, R. The hot summer of 2010: redrawing the temperature record map of Europe. *Science* **332**, 220–224 (2011).
- Russo, S., Sillmann, J. & Fischer, E. M. Top ten European heatwaves since 1950 and their occurrence in the coming decades. *Environ. Res. Lett.* **10**, 124003 (2015).
- Meng, Y., Hao, Z. C., Zhang, Y. T. & Feng, S. F. The 2022-like compound dry and hot extreme in the northern hemisphere: extremeness, attribution, and projection. *Atmos. Res.* **295**, 107009 (2023).
- Yu, R. & Zhai, P. M. More frequent and widespread persistent compound drought and heat event observed in China. *Sci. Rep.* **10**, 14576 (2020).
- Manning, C. et al. Soil moisture drought in Europe: a compound event of precipitation and potential evapotranspiration on multiple time scales. *J. Hydrometeorol.* **19**, 1255–1271 (2018).
- Li, W., Jiang, Z. H., Li, L. Z. X., Luo, J. J. & Zhai, P. M. Detection and attribution of changes in summer compound hot and dry events over northeastern China with CMIP6 models. *J. Meteorol. Res.* **36**, 37–48 (2022).
- Zscheischler, J. & Lehner, F. Attributing compound events to anthropogenic climate change. *Bull. Am. Meteorol. Soc.* **103**, E936–E953 (2022).

23. Ma, F. & Yuan, X. When will the unprecedented 2022 summer heat waves in Yangtze River basin become normal in a warming climate? *Geophys. Res. Lett.* **50**, e2022GL101946 (2023).
24. Pan, R. Y., Li, W., Wang, Q. R. & Ailiyaer, A. Detectable anthropogenic intensification of the summer compound hot and dry events over global land areas. *Earths Future* **11**, e2022EF003254 (2023).
25. Zhang, Y., Hao, Z. C., Zhang, X. & Hao, F. H. Anthropogenically forced increases in compound dry and hot events at the global and continental scales. *Environ. Res. Lett.* **17**, 024018 (2022).
26. Tang, S. K. et al. Linkages of unprecedented 2022 Yangtze River valley heatwaves to Pakistan flood and triple-dip La Nina. *Npj Clim. Atmos. Sci.* **6**, 44 (2023).
27. Ballester, J. et al. Heat-related mortality in Europe during the summer of 2022. *Nat. Med.* **29**, 1857–1866 (2023).
28. Williams, A. P., Cook, B. I. & Smerdon, J. E. Rapid intensification of the emerging southwestern North American megadrought in 2020–2021. *Nat. Clim. Change* **12**, 232–234 (2022).
29. Zhang, D. Q., Chen, L. J., Yuan, Y., Zuo, J. Q. & Ke, Z. J. Why was the heat wave in the Yangtze River valley abnormally intensified in late summer 2022? *Environ. Res. Lett.* **18**, 034014 (2023).
30. Ministry of Emergency Management of People's Republic of China (MEMC). *Monthly National Natural Disasters in August 2022* https://www.mem.gov.cn/xw/yjglbgzdt/202209/t20220917_422674.shtml (2022).
31. Zhang, L. X. et al. Understanding and attribution of extreme heat and drought events in 2022: current situation and future challenges. *Adv. Atmos. Sci.* **40**, 1941–1951 (2023).
32. Xu, Y. et al. A daily temperature dataset over china and its application in validating a RCM simulation. *Adv. Atmos. Sci.* **26**, 763–772 (2009).
33. Wu, J. & Gao, X. J. A gridded daily observation dataset over China region and comparison with the other datasets. *Chin. J. Geophys.* **56**, 1102–1111 (2013).
34. Eyring, V. et al. Overview of the coupled model intercomparison project phase 6 (CMIP6) experimental design and organization. *Geosci. Model. Dev.* **9**, 1937–1958 (2016).
35. O'Neill, B. C. et al. The scenario model intercomparison project (ScenarioMIP) for CMIP6. *Geosci. Model. Dev.* **9**, 3461–3482 (2016).
36. Liu, Y. J. et al. The January 2021 cold air outbreak over eastern China: Is there a human fingerprint? *Bull. Am. Meteorol. Soc.* **103**, S50–S54 (2022).
37. Hu, T., Sun, Y., Zhang, X. B. & Wang, D. Q. Anthropogenic Influence on the 2021 wettest september in northern China. *Bull. Am. Meteorol. Soc.* **104**, E243–E248 (2023).
38. Zscheischler, J. & Seneviratne, S. I. Dependence of drivers affects risks associated with compound events. *Sci. Adv.* **3**, e1700263 (2017).
39. Hao, Z. C., Hao, F. H., Xia, Y. L., Singh, V. P. & Zhang, X. A monitoring and prediction system for compound dry and hot events. *Environ. Res. Lett.* **14**, 114034 (2019).
40. AghaKouchak, A., Cheng, L. Y., Mazdizyasni, O. & Farahmand, A. Global warming and changes in risk of concurrent climate extremes: insights from the 2014 California drought. *Geophys. Res. Lett.* **41**, 8847–8852 (2014).
41. Cheng, L. Y. et al. How has human-induced climate change affected California drought risk? *J. Clim.* **29**, 111–120 (2016).
42. Li, H. X., Chen, H. P., Wang, H. J., Sun, J. Q. & Ma, J. H. Can Barents Sea Ice Decline in spring enhance summer hot drought events over northeastern China? *J. Clim.* **31**, 4705–4725 (2018).
43. Nelsen, R. B., Quesada-Molina, J. J., Rodríguez-Lallena, J. A. & Ubeda-Flores, M. On the construction of copulas and quasi-copulas with given diagonal sections. *Insur. Math. Econom.* **42**, 473–483 (2008).
44. Mathier, L., Perreault, L., Bobée, B. & Ashkar, F. The use of geometric and gamma-related distributions for frequency analysis of water deficit. *Stoch. Hydrol. Hydraul.* **6**, 239–254 (1992).
45. Shiau, J. T. & Shen, H. W. Recurrence analysis of hydrologic droughts of differing severity. *J. Water Resour. Plan. Manag. ASCE* **127**, 30–40 (2001).
46. Shiau, J. T. Fitting drought duration and severity with two-dimensional copulas. *Water Resour. Manag.* **20**, 795–815 (2006).
47. Mirabbasi, R., Fakheri-Fard, A. & Dinpashoh, Y. Bivariate drought frequency analysis using the copula method. *Theor. Appl. Climatol.* **108**, 191–206 (2012).
48. Zwiers, F. W., Zhang, X. B. & Feng, Y. Anthropogenic influence on long return period daily temperature extremes at regional scales. *J. Clim.* **24**, 881–892 (2011).
49. Wang, Z., Jiang, Y. J., Wan, H., Yan, J. & Zhang, X. B. Detection and attribution of changes in extreme temperatures at regional scale. *J. Clim.* **30**, 7035–7047 (2017).
50. Coles, S. G. *An Introduction to Statistical Modeling of Extreme Values* (Springer, 2001).
51. Hosking, J. R. M. L-moments: analysis and estimation of distributions using linear combinations of order statistics. *J. Roy. Stat. Soc.* **52**, 105–124 (1990).
52. Li, C., Zwiers, F., Zhang, X. B. & Li, G. L. How much information is required to well constrain local estimates of future precipitation extremes? *Earths Future* **7**, 11–24 (2019).
53. Stott, P. A., Stone, D. A. & Allen, M. R. Human contribution to the European heatwave of 2003. *Nature* **432**, 610–614 (2004).
54. Alexander, L. V. et al. Global observed changes in daily climate extremes of temperature and precipitation. *J. Geophys. Res. Atmos.* **111**, D05109 (2006).
55. Tebaldi, C., Hayhoe, K., Arblaster, J. M. & Meehl, G. A. Going to the extremes—an intercomparison of model-simulated historical and future changes in extreme events. *Clim. Change* **82**, 233–234 (2007).
56. He, C., Zhou, T. J., Zhang, L. X., Chen, X. L. & Zhang, W. X. Extremely hot east Asia and flooding western south Asia in the summer of 2022 tied to reversed flow over Tibetan plateau. *Clim. Dyn.* **61**, 2103–2119 (2023).
57. Hua, W. J., Dai, A. G., Qin, M. H., Hu, Y. H. & Cui, Y. Z. How unexpected was the 2022 summertime heat extremes in the middle reaches of the Yangtze river? *Geophys. Res. Lett.* **50**, e2023GL104269 (2023).
58. Wang, Z. Q., Luo, H. L. & Yang, S. Different mechanisms for the extremely hot central-eastern China in July–August 2022 from a Eurasian large-scale circulation perspective. *Environ. Res. Lett.* **18**, 024023 (2023).

Acknowledgements

We acknowledge the support of the Innovation Group Project of Southern Marine Science and Engineering Guangdong Laboratory (Zhuhai) (No.SML2023SP208), the Guangdong Major Project of Basic and Applied Basic Research (2020B0301030004), the National Natural Science Foundation of China (U21A6001, 42175173, and 42175028), CMA Key Open Laboratory of Transforming Climate Resources to Economy (2023002K), the Joint Open Project of KLME & CIC-FEMD, NUIST (KLME202103), and the Natural Science Basic Research Program of Shaanxi Province (grant no. 2023-JC-YB-252).

Author contributions

S.Q. and G.F. conceived the idea for the study, and D.C. downloaded the data, made the calculations, and created the figures. D.C. and S.Q. wrote the paper, and J.Y., S.T., and D.Z. contributed to the revision. All authors discussed the results throughout the whole process.

Competing interests

The authors declare no competing interests.

Additional information

Supplementary information The online version contains supplementary material available at <https://doi.org/10.1038/s41612-024-00720-3>.

Correspondence and requests for materials should be addressed to Shaobo Qiao.

Reprints and permissions information is available at <http://www.nature.com/reprints>

Publisher's note Springer Nature remains neutral with regard to jurisdictional claims in published maps and institutional affiliations.

Open Access This article is licensed under a Creative Commons Attribution 4.0 International License, which permits use, sharing, adaptation, distribution and reproduction in any medium or format, as long as you give appropriate credit to the original author(s) and the source, provide a link to the Creative Commons licence, and indicate if changes were made. The images or other third party material in this article are included in the article's Creative Commons licence, unless indicated otherwise in a credit line to the material. If material is not included in the article's Creative Commons licence and your intended use is not permitted by statutory regulation or exceeds the permitted use, you will need to obtain permission directly from the copyright holder. To view a copy of this licence, visit <http://creativecommons.org/licenses/by/4.0/>.

© The Author(s) 2024